AGU PUBLICATIONS

Geophysical Research Letters

RESEARCH LETTER
10.1002/2017GL075592

Key Points:
- Noise interferometry allows accurate determination of the velocity structure at 3 km depth from anthropogenic noise at the surface
- *P* and *S* velocity profiles along a borehole in the Groningen reservoir were accurately retrieved by noise interferometry
- Shear wave anisotropy was detected with a magnitude of (4 ±2)% and a fast polarization direction of N65°W±18°

Supporting Information:
- Supporting Information S1

Correspondence to:
W. Zhou,
w.zhou@uu.nl

Citation:
Zhou, W., & Paulssen, H. (2017). *P* and *S* velocity structure in the Groningen gas reservoir from noise interferometry. *Geophysical Research Letters*, *44*, 11,785–11,791. https://doi.org/10.1002/2017GL075592

Received 11 SEP 2017
Accepted 10 NOV 2017
Accepted article online 13 NOV 2017
Published online 8 DEC 2017

P and *S* Velocity Structure in the Groningen Gas Reservoir From Noise Interferometry

Wen Zhou[1] **and Hanneke Paulssen**[1]

[1] Department of Earth Sciences, Utrecht University, Utrecht, Netherlands

Abstract Noise interferometry has proven to be a powerful tool to image seismic structure. In this study we used data from 10 geophones located in a borehole at ~3 km depth within the Groningen gas reservoir in the Netherlands. The continuous data cross correlations show that noise predominantly comes in from above. The observed daily and weekly variations further indicate that the noise has an anthropogenic origin. The direct *P* wave emerges from the stacked vertical component cross correlations with frequencies up to 80 Hz and the direct *S* wave is retrieved from the horizontal components with frequencies up to 50 Hz. The measured intergeophone travel times were used to retrieve the *P* and *S* velocity structure along the borehole, and a good agreement was found with well log data. In addition, from the *S* wave polarizations, we determined azimuthal anisotropy with a fast direction of N65°W±18° and an estimated magnitude of (4±2)%. The fast polarization direction corresponds to the present direction of maximum horizontal stress measured at nearby boreholes but is also similar to the estimated paleostress direction.

1. Introduction

The Groningen gas field (Figure 1a) in the Netherlands is one of the world's largest onshore gas fields and has been producing since 1963 (van Thienen-Visser & Breunese, 2015). As a result of gas extraction, subsidence and induced seismicity occur, causing damage and concern in the area.

In 2013, the year with the highest level of induced seismicity, two geophone strings were placed in two boreholes that were originally used as production wells, to monitor seismicity in the reservoir (Nederlandse Aardolie Maatschappij, 2016). A string of 10 geophones was positioned in borehole SDM-1 and a string of 7 geophones in borehole ZRP-1 (Figure 1b). In this study we used the data of SDM-1 to demonstrate that it is possible to accurately determine the *P* and *S* wave velocity structure along a borehole at 3 km depth, as well as *S* wave anisotropy, from anthropogenic noise at the surface using seismic interferometry.

The technique of seismic interferometry is well established. A number of studies has shown that the Green's function between two receivers can be extracted from noise cross correlations (e.g., Bakulin & Calvert, 2006; Snieder, 2004; Wapenaar & Fokkema, 2006; Weaver & Lobkis, 2005). Some conditions apply, such as an isotropic distribution of noise sources, although in practice noise sources within the receiver-receiver Fresnel zones suffice (Snieder & Larose, 2013). The technique has been used widely: to retrieve surface waves for imaging crustal and upper mantle structure (e.g., Galetti et al., 2017; Lin et al., 2011; Shapiro et al., 2005), to detect body waves traveling through the mantle and core (e.g., Gerstoft et al., 2008; Poli et al., 2012; Wang et al., 2015), in exploration settings (e.g., Draganov et al., 2009; Vasconcelos et al., 2010), and to image time-dependent variations of the velocity field (e.g., Brenguier et al., 2008; de Ridder et al., 2014; Draganov et al., 2012; Hillers et al., 2015; Wegler & Sens-Schönfelder, 2007). An extensive review of the literature is given in Snieder and Larose (2013).

Some studies obtained the velocity structure between borehole sensors using earthquake data (Hofman et al., 2017; Nakata & Snieder, 2012; Trampert et al., 1993), while recent studies have shown that borehole body wave propagation can also be retrieved from noise data. Miyazawa et al. (2008) extracted direct downgoing *P* and *S* waves up to 370 m depth in the frequency band 10–55 Hz from industrial noise at the surface. Grechka and Zhao (2012) summarized several applications of downhole seismic interferometry. They obtained a downgoing *P* wave with frequencies up to 50 Hz at nearly 2 km depth and also found horizontally propagating *S* waves between two boreholes. Vaezi and Van der Baan (2015) investigated the effects geophone clamping to the borehole. They retrieved downgoing *P* waves at 1,800 m depth and in some cases also more weakly upgoing

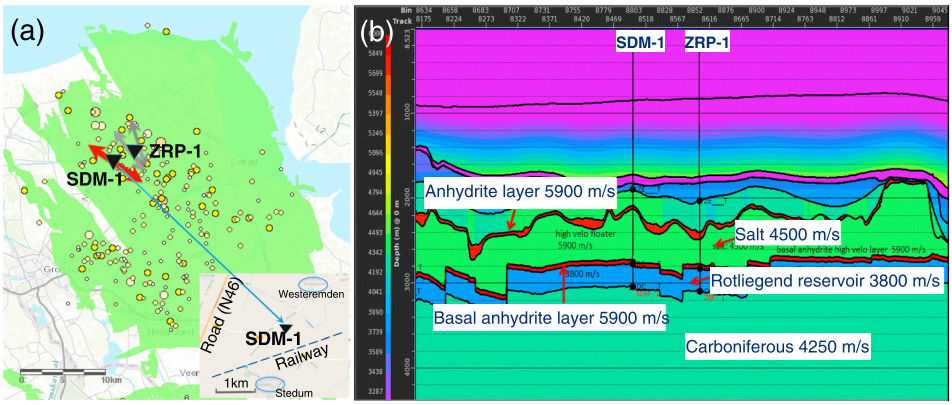

Figure 1. (a) The Groningen gas field (green) with seismicity (M_L 0.1 – 3.5; 2013 – 2014) and the borehole locations SDM-1 and ZRP-1(black inverted triangles). The grey arrows indicate the maximum horizontal stress directions in boreholes ZRP-2 and ZRP-3 from breakout tests (van Eijs, 2015). The red arrow indicates the fast *S* wave polarization direction obtained for SDM-1 in this study. Inset shows the location of borehole SDM-1 with the village of Westeremden, the railway, and the road N46. (b) Cross section (length ~20 km, depth 4.4 km) through a *P* wave velocity model with boreholes SDM-1 and ZRP-1. The velocity scale bar ranges from 3,287 to 6,000 m/s. (Source: Nederlandse Aardolie Maatschappij, NAM).

P waves at frequencies lower than 60 Hz. Recently, Behm (2016) found downgoing *P* and *S* waves up to 50 Hz at around 1,000 m depth and suggested that velocity changes may be monitored from the high-frequency (> 50 Hz) part of the cross correlations.

In this study, noise interferometry was applied to the three component recordings measured in borehole SDM-1. The *P* and *S* wave velocity structure within the reservoir was determined with high accuracy, and azimuthal anisotropy was detected from the obtained *S* wave polarizations.

2. Data and Processing

We used 33 days of data (21 November to 23 December 2013) from the ten 15 Hz geophones in borehole SDM-1 positioned at depths from 2,750 m to 3,017 m with a geophone spacing 30 m. The data were continuously recorded with a sampling rate of 2,000 Hz. The data from the original sensor directions were rotated to east, south and down, using the information provided by check shots.

To obtain the cross correlations, we followed the processing scheme of Bensen et al. (2007), using 1 bit normalization to remove amplitude bias in the time domain. Spectral whitening with a smoothed version of the amplitude spectrum was applied to remove frequency bias. After that the data were filtered from 3 to 400 Hz. We deliberately used a wide band-pass filter to allow potential additional filtering at later stages. We tested that there is only little difference in filtering before or after cross correlation (see Figure S1 in the supporting information).

Normalized cross correlations $C_{rs}(t)$ were calculated for each geophone pair:

$$C_{rs}(t) = \frac{\int_{-T/2}^{T/2} r(\tau)s(\tau + t)\mathrm{d}\tau}{\| r(t) \| \| s(t) \|}$$

where $s(t)$ is the processed record at the reference geophone (i.e., virtual source), and $r(t)$ is processed record at one of the other (receiver) geophones. T is the duration of the segmented records, and $\|\|$ denotes the L^2 norm of the signal. The cross correlations were calculated for 6 s segments ($T = 6$ s) with two thirds overlap, and then they were stacked per hour. Further processing was based on these hourly stacks.

3. Cross Correlations

The cross correlations obtained from 24 h of stacked data with the top geophone as virtual source are displayed in Figure 2. The causal parts of the cross correlations between the vertical components (Figure 2a) show a strong signal with an apparent velocity of about 3,700 m/s, similar to the average *P* wave velocity of the (Rotliegend) reservoir (see Figure 1b). It is therefore interpreted as the direct downgoing *P* wave.

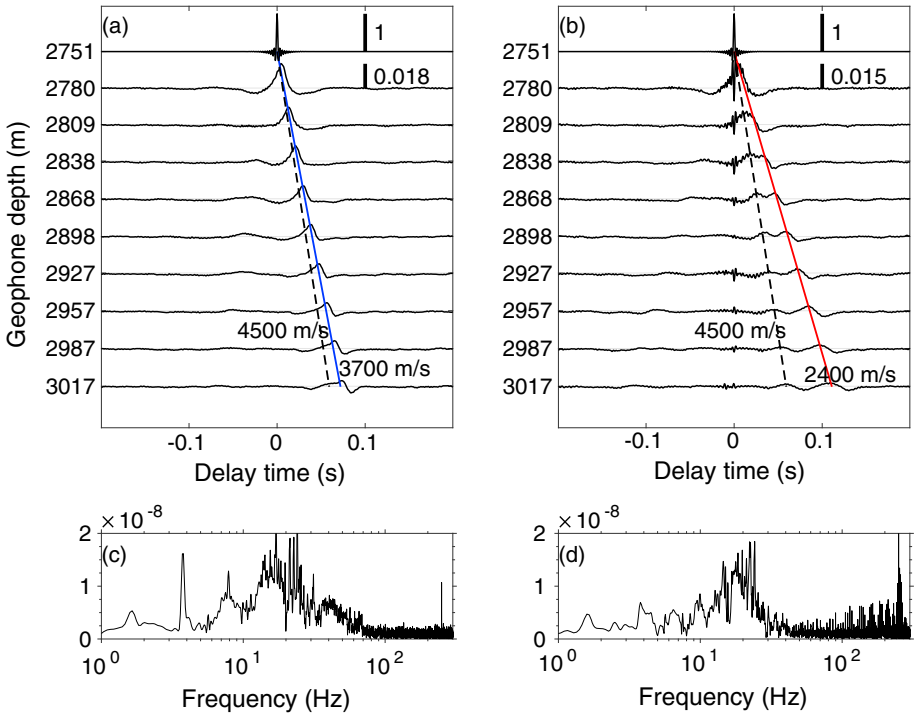

Figure 2. (a) Vertical (Z-Z) component cross correlations and (b) east (E-E) component cross correlations for the 24 h stacks of 21 November 2013. The top geophone was used as virtual source. The vertical bars indicate the scaling of the top trace (with value 1) and the other traces (with 0.018 and 0.015, respectively). (c and d) The power spectra of the vertical and east component cross correlations for the lowermost geophone, respectively.

The cross correlations between the east components show a signal with an apparent velocity of about 2,400 m/s (Figure 2b). This velocity is similar to the average *S* wave in the reservoir (courtesy of Nederlandse Aardolie Maatschappij, NAM; see Figure 4) and is therefore interpreted as the downgoing *S* wave. Full sets of cross correlations between all components can be found in Figures S2 and S3 of the supporting information, for the top and bottom geophone as virtual source respectively. The *P* wave has its largest amplitude on the vertical component cross correlations, whereas the east and north component cross correlations have their strongest amplitude at the arrival time of the *S* wave (where the vertical component has near-zero amplitude). This is consistent with the polarization of vertical *P* wave and *S* wave propagation along the borehole, respectively. The strong signals for the downgoing waves compared to the upgoing ones indicate that the dominant noise comes from above.

The power spectra (Figures 2c and 2d) show that the vertical component cross correlations contain signal with frequencies up to 80 Hz, whereas the horizontal component cross correlations only contain signal up to 50 Hz.

Apart from the direct *P* and *S* waves, the horizontal and vertical component cross correlations seem to contain an additional signal with an apparent velocity of ~4,500 m/s. It is most clearly seen on the horizontal components but can also be identified as a small precursory onset to the *P* wave on the vertical component cross correlations. We interpret this signal as a *P* wave that comes in at an inclined angle, because its apparent velocity is higher than the *P* velocity of the medium and also because it is observed on the vertical and horizontal cross correlations. We also identify high-frequency arrivals at 0 s delay time on all cross correlations. Here they are most clearly visible on the east component cross correlations, but their signature can also be identified in the spectra at around 250 Hz. Such signals have been identified before and were then attributed to tiny time calibration pulses superposed on the recordings by the data logger (Takagi et al., 2015).

Figures 3a and 3b show the causal parts of the hourly cross correlations as a function of day and time over the entire period of 33 days for the vertical and east component, respectively. The top geophone is used as virtual source and the bottom geophone as receiver. Diurnal and weekly variations of the cross correlations can be identified, revealing that the downward propagating noise is of anthropogenic origin. A zoom-in of this figure for a single day is given in Figure S4 of the supporting information.

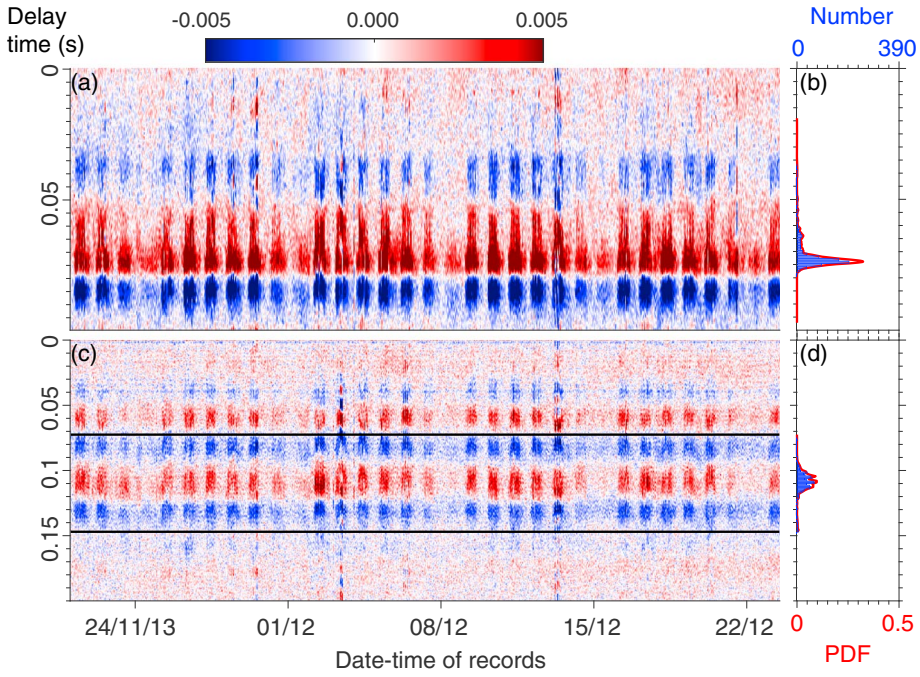

Figure 3. (a) Causal parts of the vertical component cross correlations with the top geophone as virtual source and the bottom geophone as receiver. (b) Histogram of the number of apparent *P* wave arrival times (blue) with its PDF (red) in the same figure. (c) Similar to Figure 3a but for east component cross correlations with the black lines indicating timing thresholds. (d) Similar to Figure 3b but for *S* wave arrival times.

4. Travel Time Estimation and Velocity Profile

To obtain a single accurate apparent *P* wave travel time per geophone pair, the time of maximum vertical component cross correlation was measured for each of the hourly stacks (Figure 3a). With 33 days and 24 h per day, we obtained 33*24 *P* wave travel times for each geophone pair. The histogram of travel times for Figure 3a is shown in Figure 3b (blue distribution). Because the travel time distribution is skewed, we used a kernel density estimation (Botev et al., 2010) to obtain its probability density function (PDF) (Figure 3b, red curve). The maximum likelihood value obtained from this PDF is then used as estimate of the travel time for this geophone pair. In a similar way, using each of the geophones as a virtual source and the others as receiver, in total 45 independent source-receiver travel times were obtained. The total travel time for each virtual source-receiver pair can be written as the summation of interval travel times between neighboring pairs of geophones. A linear least squares method was used to the 45 source-receiver travel times (equations) to determine the 9 interval travel times (unknowns). Estimates of the errors in the interval travel times were obtained from the diagonal elements of the model covariance matrix. The velocities between the geophones (with their errors) were directly calculated from the interval travel times (with their errors) using the intergeophone distance of 30 m.

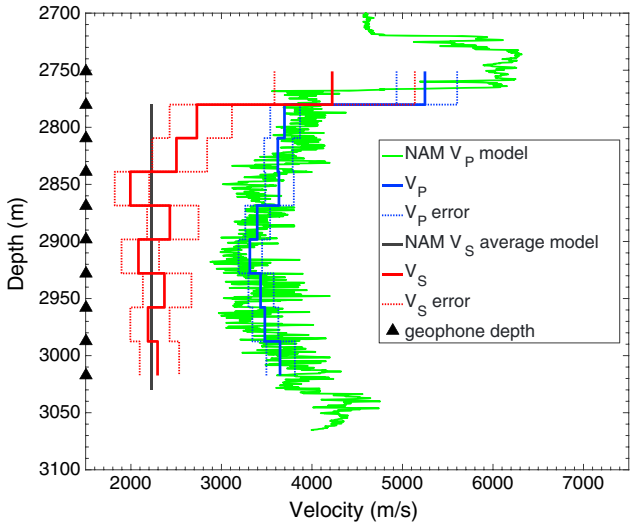

Figure 4. Inferred *P* velocity profile (blue) and *S* velocity profile (red) with errors (dashed). The *P* velocity from well log data is shown in green and the average reservoir *S* velocity in black (data provided by NAM). Geophone depths are indicated by triangles.

The same approach was used for the east components to obtain the *S* wave velocities. However, in order to reduce the influence from the earlier *P* wave arrival, we set timing thresholds with apparent velocities of 1,500 m/s and 3,500 m/s for *S* wave picking. Furthermore, not all timings could be used due to interference with this earlier arrival (Figure 2b). Therefore, only geophones with distances larger than 90 m to the virtual source were used.

The inferred *P* and *S* velocity profiles are shown in Figure 4. We find a good agreement between our estimated *P* velocity structure and the velocity structure from acoustic logging (courtesy of NAM) with lower velocities in

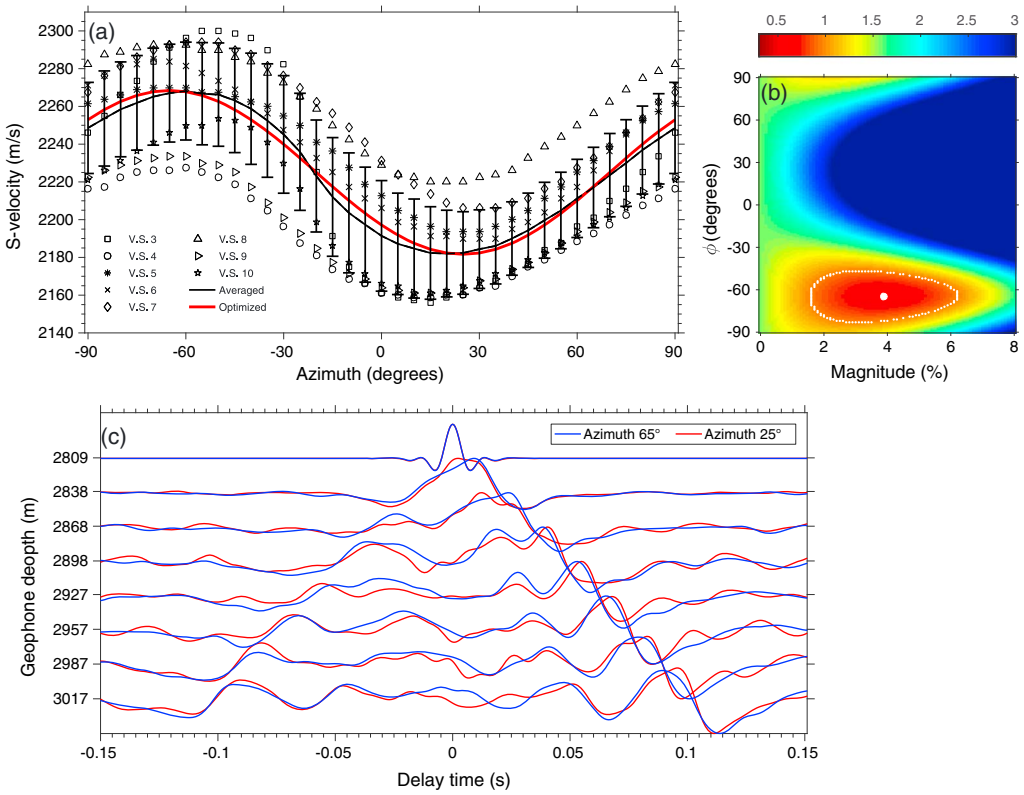

Figure 5. (a) Shear velocity as a function of azimuth for the eight virtual sources (various symbols). The average is represented by the black solid curve, and the standard deviations are indicated by the vertical bars. The optimum fit to the data ($M = 4\%$, $\phi = -65°$) is shown by the red curve. (b) χ^2 misfit as a function of azimuth of the fast direction and magnitude. The white line represents the χ^2=1 contour. (c) Horizontal component cross correlations for azimuth N65°W (fast, blue) and N25°E (slow, red) for a virtual source at 2,809 m.

the middle of the reservoir. The top geophone is located in an anhydrite layer, and the corresponding high velocity is recovered in our model. The *S* velocity structure shows a sharp decrease at the top, but the velocity structure within the reservoir is more poorly resolved. However, there is a good agreement with the average *S* velocity of the reservoir sandstone as provided by the NAM.

5. Shear Wave Anisotropy

Shear wave anisotropy can be used to detect preferred alignment in materials, such as oriented cracks caused by the local stress situation. Miyazawa et al. (2008) successfully retrieved shear wave anisotropy in a borehole by comparing time shifts of the cross correlations for different azimuths. In this study, we followed a similar approach to determine polarization anisotropy within the reservoir sandstone. We used data from the reservoir only, that is, from the third to the tenth geophone (2,809–3,017 m), and stacked the cross correlations over the entire period of 33 days. The horizontal components were rotated over 90° with 5° increments to obtain cross-correlation traces for 37 azimuths between −90° (west-west cross correlations) and 90° (east-east cross correlations). The data were band-pass filtered between 3 and 100 Hz to eliminate high-frequency noise. For each of the azimuths, the shear wave velocity was obtained from the optimum stacking velocity along the eight cross-correlation traces. The optimum stacking velocity is the velocity that best aligns the *S* wave arrivals, giving the largest amplitude on the summed trace. The process was applied using each of the geophones as a virtual source. Figure 5a shows the shear wave velocity as a function of azimuth for each of the virtual sources (indicated by different symbols). For each azimuth the average shear wave velocity with its standard deviation is obtained from these data. Clearly, the data are suggestive of shear wave splitting showing a 2-ψ dependence with a 90° difference between the fast and slow polarization directions. The average shear velocity V_S as a function of azimuth ψ is thus fitted as

$$V_S(\psi) = V_{S_0}\left[1 + \frac{1}{2}M\cos(2(\psi - \phi))\right] \quad (1)$$

where V_{S_0} is the azimuth-independent shear wave velocity of 2,225 m/s, ϕ the fast polarization direction, and M the magnitude of shear wave anisotropy defined as $(V_{S_{\text{fast}}} - V_{S_{\text{slow}}})/V_{S_0}$. We carried out a grid search for ϕ and M to find the optimum parameters using a χ^2 misfit

$$\chi^2 = \frac{1}{N}\sum_{i=1}^{N}\frac{(d_i^{\text{obs}} - d_i^{\text{calc}})^2}{\sigma_i^2}$$

where the observed data d_i^{obs} is $V_S(\psi_i)$ with its standard deviation σ_i shown in Figure 5a, and d_i^{calc} is obtained from equation (1). Figure 5b shows that the optimum value is obtained for a magnitude of 4% and a fast polarization direction of −65° (N65°W). The uncertainties are inferred from the χ^2=1 contour, giving a magnitude of the anisotropy of (4±2)% with a fast polarization direction of N65°W±18°. This direction is not only consistent with the NW-SE paleostress directions found for the Groningen reservoir (van Gent et al., 2009) but also with the current maximum horizontal stress directions determined at two nearby boreholes (van Eijs, 2015; see Figure 1a). Figure 5c shows the cross correlations for the fast and slow directions using the geophone at 2,809 m depth as virtual source.

6. Discussion and Conclusions

In this study, we analyzed noise data from 10 geophones located at ∼3 km depth in the Groningen gas reservoir in the Netherlands. Vertical component cross correlations for 33 days of continuous recording clearly show direct *P* arrivals in 3–80 Hz band, whereas the horizontal components yield *S* arrivals at 3–50 Hz (Figure 2). We observe that the cross correlations are dominated by noise from above and show both diurnal and weekly variations (Figure 3). This indicates that the fluctuations are due to variations in anthropogenic noise. Previous studies by Grechka and Zhao (2012), Vaezi and Van der Baan (2015) and Behm (2016) have shown that surface activity can indeed be the dominant noise source up to 2 km depth. Our results confirm their observation, extending it to a depth of 3 km. Traffic can be an important source of noise; it has been employed in other interferometry studies (Behm et al., 2014; Nakata et al., 2011; Quiros et al., 2016). The effects of traffic, from the national road N46 and the railroad (Figure 1), also dominate our noise recordings at depth. Analyzing the noise spectra as a function of time, we found that relatively high-frequency noise was generated at regular times corresponding to the train schedule (Figure S5 in the supporting information), suggesting that the train signal is an important source of high-frequency noise. Traffic along the road N46 is another likely noise source as revealed by the precursory *P* wave signal on the horizontal and vertical cross correlations (Figure 2). Assuming wave propagation along a straight line from the road at ∼1,800 m distance to the borehole at 3 km depth, we find that the signal would come in at an angle of 31° with the vertical. Using a *P* wave velocity of 3,700 m/s in the medium, this would give an apparent velocity of 4,300 m/s, very close to the 4,500 m/s observed for the precursory arrival. It may seem surprising that we obtained strong *P* wave and *S* wave cross-correlation peaks at the "correct" travel times corresponding to downward propagation along the borehole, considering that traffic noise is generated at some horizontal distance. We note, however, that subsurface scattering likely plays an important role and that constructive interference from randomly distributed noise sources is maximum in the stationary phase region (Snieder, 2004; Snieder & Larose, 2013), that is along the borehole in this case.

In this study we obtained the *P* wave and *S* wave travel times between each geophone pair, we used the 33(days)*24(h) travel times picked from hourly stacked cross correlations and determined the most likely travel times from the measurement distribution. The difference between this measurement and the maximum cross-correlation time obtained for the entire 33 day stack is within one sample (0.5 ms).

We also found evidence for shear wave anisotropy, estimating the average shear velocity within the reservoir as a function of polarization direction. The anisotropy amounts to (4±2)% with a fast direction of N65°W±18°. The orientation is roughly similar to the NW-SE paleostress direction as well as directions of maximum horizontal stress determined at nearby boreholes, so the origin of the anisotropy remains ambiguous. Although magnitudes of shear wave anisotropy and stress anisotropy cannot directly be related, we note that the magnitude of anisotropy (∼4%) and the difference between the maximum and minimum horizontal stress at nearby wells (∼3%) (van Eijs, 2015) are both small.

This study has shown that the correlation of anthropogenic noise with frequencies up to 80 Hz can be used to determine the velocity structure along a borehole at 3 km depth. The scattered wavefield produced by traffic on a nearby road and railroad likely allowed the accurate construction of the velocity profile. This opens perspectives for other (former production) boreholes with similar noise settings for which the velocity structure

or anisotropy is insufficiently known. We did not succeed to identify temporal variations of the medium within the 33 day time span because the cross correlations appeared to be dominated by fluctuations in anthropogenic noise (Figures 3 and S4 in the supporting information). Nevertheless, it should be possible to identify temporal medium variations at locations with more stable noise environments, as shown by Behm (2016).

Acknowledgments
We thank the NAM with Remco Romijn for providing us with the data. Elmer Ruigrok is thanked for helpful discussions, and Michael Behm, Sjoerd de Ridder, and an anonymous reviewer for their comments that helped to improve the paper. This project has been funded by the European Union's Horizon 2020 research and innovation programme under the Marie Sklodowska-Curie grant agreement 642029-ITN CREEP. The data that were used in this study are not publicly available but may be requested at the Nederlandse Aardolie Maatschappij.

References

Bakulin, A., & Calvert, R. (2006). The virtual source method: Theory and case study. *Geophysics*, *71*(4), SI139–SI150.
Behm, M. (2016). Feasibility of borehole ambient noise interferometry for permanent reservoir monitoring. *Geophysical Prospecting*, *65*, 563–580.
Behm, M., Leahy, G. M., & Snieder, R. (2014). Retrieval of local surface wave velocities from traffic noise—An example from the La Barge basin (Wyoming). *Geophysical Prospecting*, *62*(2), 223–243.
Bensen, G., Ritzwoller, M., Barmin, M., Levshin, A., Lin, F., Moschetti, M., … Yang, Y. (2007). Processing seismic ambient noise data to obtain reliable broad-band surface wave dispersion measurements. *Geophysical Journal International*, *169*(3), 1239–1260.
Botev, Z. I., Grotowski, J. F., & Kroese, D. P. (2010). Kernel density estimation via diffusion. *The Annals of Statistics*, *38*(5), 2916–2957.
Brenguier, F., Campillo, M., Hadziioannou, C., Shapiro, N., Nadeau, R. M., & Larose, E. (2008). Postseismic relaxation along the San Andreas fault at Parkfield from continuous seismological observations. *Science*, *321*(5895), 1478–1481.
de Ridder, S., Biondi, B., & Clapp, R. (2014). Time-lapse seismic noise correlation tomography at Valhall. *Geophysical Research Letters*, *41*, 6116–6122. https://doi.org/10.1002/2014GL061156
Draganov, D., Campman, X., Thorbecke, J., Verdel, A., & Wapenaar, K. (2009). Reflection images from ambient seismic noise. *Geophysics*, *74*, A63–67.
Draganov, D., Heller, K., & Ghose, R. (2012). Monitoring CO_2 storage using ghost reflections retrieved from seismic interferometry. *International Journal of Greenhouse Gas Control*, *11*, S35—S46.
Galetti, E., Curtis, A., Baptie, B., Jenkins, D., & Nicolson, H. (2017). Transdimensional Love-wave tomography of the British Isles and shear-velocity structure of the East Irish Sea Basin from ambient-noise interferometry. *Geophysical Journal International*, *208*(1), 36–58.
Gerstoft, P., Shearer, P. M., Harmon, N., & Zhang, J. (2008). Global *P*, *PP*, and *PKP* wave microseisms observed from distant storms. *Geophysical Research Letters*, *35*, L23306. https: //doi.org/10.1029/2008GL036111
Grechka, V., & Zhao, Y. (2012). Microseismic interferometry. *The Leading Edge*, *31*(12), 1478–1483.
Hillers, G., Husen, S., Obermann, A., Planès, T., Larose, E., & Campillo, M. (2015). Noise-based monitoring and imaging of aseismic transient deformation induced by the 2006 Basel reservoir stimulation. *Geophysics*, *80*(4), KS51–KS68.
Hofman, R., Ruigrok, E., Dost, B., & Paulssen, H. (2017). A shallow seismic velocity model for the Groningen area in the Netherlands. *Journal of Geophysical Research: Solid Earth*, *122*, 1–16. https://doi.org/10.1002/2017JB014419
Lin, F.-C., Ritzwoller, M. H., Yang, Y., Moschetti, M. P., & Fouch, M. (2011). Complex and variable crustal and uppermost mantle seismic anisotropy in the western United States. *Nature Geoscience*, *4*, 1239–1260.
Miyazawa, M., Snieder, R., & Venkataraman, A. (2008). Application of seismic interferometry to extract *P*-and *S*-wave propagation and observation of shear-wave splitting from noise data at Cold Lake, Alberta, Canada. *Geophysics*, *73*(4), D35–D40.
Nakata, N., & Snieder, R. (2012). Estimating near-surface shear wave velocities in Japan by applying seismic interferometry to KiK-net data. *Journal of Geophysical Research*, *117*, B01308. https://doi.org/10.1029/2011JB008595
Nakata, N., Snieder, R., Tsuji, T., Larner, K., & Matsuoka, T. (2011). Shear wave imaging from traffic noise using seismic interferometry by cross-coherence. *Geophysics*, *76*(6), SA97–SA106.
Nederlandse Aardolie Maatschappij (2016). Study and data acquisition plan induced seismicity in Groningen-Winningsplan 2016, *NAM Report*, (EP201604200072).
Poli, P., Campillo, M., Pedersen, H., & Group, L. W. (2012). Body-wave imaging of Earth's mantle discontinuities from ambient seismic noise. *Science*, *338*, 1063–1065.
Quiros, D. A., Brown, L. D., & Kim, D. (2016). Seismic interferometry of railroad induced ground motions: Body and surface wave imaging. *Geophysical Journal International*, *205*(1), 301–313.
Shapiro, N. M., Campillo, M., Stehly, L., & Ritzwoller, M. H. (2005). High-resolution surface-wave tomography from ambient seismic noise. *Science*, *307*(5715), 1615–1618.
Snieder, R. (2004). Extracting the Green's function from the correlation of coda waves: A derivation based on stationary phase. *Physical Review E*, *69*(4). https://doi.org/10.1103/PhysRevE.69.046610
Snieder, R., & Larose, E. (2013). Extracting Earth's elastic wave response from noise measurements. *Annual Review of Earth and Planetary Sciences*, *41*, 183–206.
Takagi, R., Nishida, K., Aoki, Y., Maeda, T., Masuda, K., Takeo, M., … Saito, K. (2015). A single bit matters: Coherent noise of seismic data loggers. *Seismological Research Letters*, *86*(3), 901–907.
Trampert, J., Cara, M., & Frogneux, M. (1993). SH propagator matrix and Qs estimates from borehole- and surface-recorded earthquake data. *Geophysical Journal International*, *112*(2), 290–299.
Vaezi, Y., & Van der Baan, M. (2015). Interferometric assessment of clamping quality of borehole geophones. *Geophysics*, *80*(6), WC89–WC98.
van Eijs, R. (2015). Neotectonic stresses in the Permian Slochteren formation of the Groningen field. *NAM Report*, (EP201510210531).
van Gent, H. W., Back, S., Urai, J. L., Kukla, P. A., & Reicherter, K. (2009). Paleostresses of the Groningen area, the Netherlands—Results of a seismic based structural reconstruction. *Tectonophysics*, *470*(1), 147–161.
van Thienen-Visser, K., & Breunese, J. (2015). Induced seismicity of the Groningen gas field: History and recent developments. *The Leading Edge*, *34*(6), 664–671.
Vasconcelos, I., Sava, P., & Douma, H. (2010). Nonlinear extended images via image-domain interferometry. *Geophysics*, *75*(6), SA105–SA115.
Wang, T., Song, X., & Xia, H. H. (2015). Equatorial anisotropy in the inner part of Earth's inner core from autocorrelation of earthquake coda. *Nature Geoscience*, *8*(3), 224–227.
Wapenaar, K., & Fokkema, J. (2006). Green's function representations for seismic interferometry. *Geophysics*, *71*(4), SI33–SI46.
Weaver, R. L., & Lobkis, O. I. (2005). Fluctuations in diffuse field-field correlations and the emergence of the Green's function in open systems. *Journal of the Acoustical Society of America*, *117*(6), 3422–3439.
Wegler, U., & Sens-Schönfelder, C. (2007). Fault zone monitoring with passive image interferometry. *Geophysical Journal International*, *168*(3), 1029–1033.